Model Wind over the Central and Southern California Coastal Ocean

HSIAO-MING HSU

National Center for Atmospheric Research,* Boulder, Colorado

LIE-YAUW OEY

Princeton University, Princeton, New Jersey

WALTER JOHNSON

Minerals Management Service, Herndon, Virginia

CLIVE DORMAN

Scripps Institution of Oceanography, La Jolla, California

RICHARD HODUR

Naval Research Laboratory, Monterey, California

ABSTRACT

Recent studies have shown the importance of high-resolution wind in coastal ocean modeling. This paper tests the Coupled Ocean–Atmosphere Mesoscale Prediction System (COAMPS) at the 9-, 27-, and 81-km grid resolutions in simulating wind off the central and southern California coasts, including the Santa Barbara Channel (SBC). The test period is March–May (1999) when the wind changes from its characteristics more typical of winter, to spring when strong gradients exist in the SBC. The model results were checked against wind station time series, Special Sensor Microwave Imager wind speeds, and the European Centre for Medium-Range Weather Forecasts (ECMWF) reanalysis. The high-resolution (9-km grid) COAMPS wind shows expansion fans downwind of major capes where speed increases. The large-scale [O(100 km)] wind turns onshore in the Southern California Bight where both wind and wind stress curl weaken southward along the coast. The formation and evolution of the Catalina eddies are also simulated. These general features agree with observations. The turning appears to be the cumulative effect of synoptic cyclones shed downwind of Point Conception during periods of intense northerly wind. The turning and eddies are much weaker in the ECMWF reanalysis or the COAMPS field at the 81-km grid. Near the coast, observed small-scale (tens of kilometers) structures are reasonably reproduced by COAMPS at the 9-km grid. Results from the 9-km grid generally compare better with observations than the 27-km grid, suggesting that a more accurate model wind may be obtained at even higher resolution. However, in the SBC, simulated winds at both the 9- and 27-km grids show along-channel coherency during May, contrary to observations. The observed winds in the channel appear to be of small localized scales ($\approx$<10 km) and would require an improved model grid and perhaps also boundary layer physics to simulate.

1. Introduction

Wind is an important forcing of the coastal oceans (Allen 1980). This is so for the Central California Shelf

Corresponding author address: Lie-Yauw Oey, AOS Program, Princeton University, Sayre Hall, Princeton, NJ 08544.
E-mail: lyo@princeton.edu

and Slope (CCSS) and Southern California Bight (SoCB), and the transition zone in between [i.e., the Santa Barbara Channel (SBC) see Fig. 1]. These are regions where the effects of wind stress curl are also important (Oey 1996, 1999; Munchow 2000). However, with a few exceptions involving aircraft measurements during limited time periods (Brink and Muench 1986; Caldwell et al. 1986; Persson et al. 2005), estimates of wind stress and wind stress curl over the CCSS–SBC–SoCB coastal zone have been based on relatively sparse buoy and land-based measurements (Dorman and
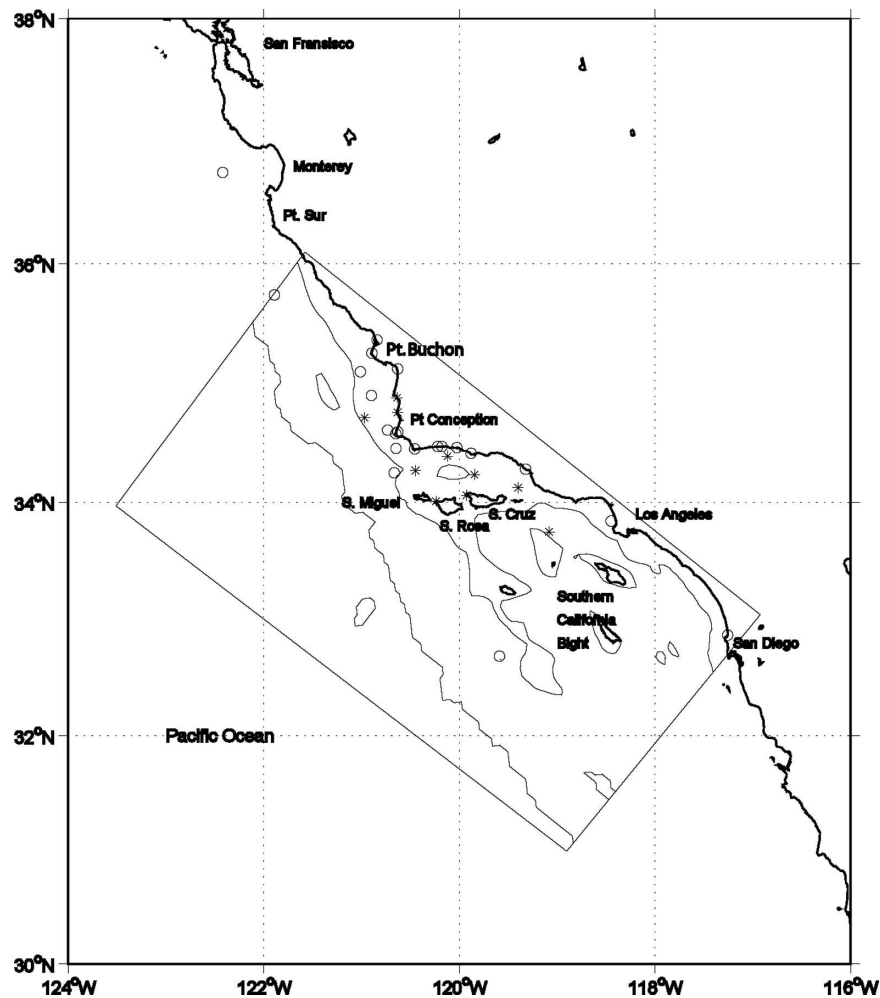
FIG. 1. A locator map of the ocean region of interest, off the California coast, including the SBC and SoCB. The rectangle is the ocean model domain used by Oey et al. (2001, 2004) and contours show the 500- and 2000-m isobaths. Open circles and asterisks denote wind stations where we have analyzed the wind data. The asterisks denote those presented in detail in the text.

Winant 1995, 2000). A comprehensive, high-resolution wind field is needed to characterize oceanographically relevant aspects of meteorological variability in the region (Samelson et al. 2002).

Winds are strong and persistently equatorward west of SBC and over the CCSS, and are weak east of SBC and in the south over the SoCB. Winant and Dorman (1997) examine winds using buoy data and also California Cooperative Oceanic Fisheries Investigation observations. Mean wind stresses west of SBC and over the CCSS exceed 0.1 N m^{-2}, but are weaker in the eastern SBC and near the coast in the SoCB. There exist significant fluctuations, from diurnal to synoptic (i.e., days; Dorman and Winant 2000). The south-southeastward wind stress at the western entrance of SBC, for example, can reach 0.2–0.3 N m^{-2}, and it de-

creases rapidly eastward over a distance of about 50 km. This rapid eastward weakening is primarily due to blockage of winds from the north by mountain ranges along the channel's northern coast. The resulting wind stress curl often exceeds 0.1 N m^{-2} (100 km)$^{-1}$ (Munchow 2000). These winds and wind stress curls are important driving agents of the regional ocean currents (Oey 1996, 1999; Wang 1997; Harms and Winant 1998; Oey et al. 2001, 2004).

Our ultimate goal is to produce a high-resolution wind field to be tested in ocean models (e.g., Oey et al. 2004; see Fig. 1 in the current paper). In this paper, we simulate winds for a 3-month period, March–May 1999, using the Coupled Ocean–Atmosphere Mesoscale Prediction System (COAMPS; Hodur 1997). The March–May period is sometimes called the "spring transition"

period during which more erratic winds due to (late) winter storms in March give way to, in May, a more typical summertime wind that is intense and persistently equatorward west of the channel, and weak farther east. This shift in the wind field has been shown to also correspond to a shift in the regional ocean dynamics (Oey et al. 2001). The chosen period is also when relatively dense network of wind stations and ocean observations are available. The specific objective is to test the capability of high-resolution Numerical Weather Prediction models such as COAMPS for simulating the low-level flow in the coastal zone proximal to a rugged terrain. Quality high-resolution wind fields are potentially important in small-scale ocean processes, and a companion paper (Dong and Oey 2005) describes ocean dynamics driven by the COAMPS winds derived herein.

Section 2 describes the COAMPS experiment and section 3 describes the results. Section 4 compares COAMPS with wind station observations, Special Sensor Microwave Imager (SSM/I) data, and also the European Centre for Medium-Range Weather Forecasts (ECMWF) reanalysis. Section 5 summarizes results of an ocean model driven by COAMPS and other winds. Section 6 discusses the Catalina eddies and expansion fans and section 7 concludes the paper.

2. COAMPS experiment: March–May 1999

COAMPS solves the compressible, nonhydrostatic equations on an Arakawa C grid, and uses the height-based terrain-following vertical coordinate grid. It includes physical parameterizations of short- and long-wave radiation (Harshvardhan et al. 1987), cumulus convection (Kain and Fritsch 1990), and subgrid-scale boundary layer processes using a level-2.5 turbulence scheme (Therry and LaCarrere 1983). Following Rutledge and Hobbs (1983), explicit moist physics contains prognostic equations of water vapor, cloud water, rainwater, cloud ice, and snowflakes. COAMPS has been extensively tested (Hodur 1997; Doyle 1997; Thompson et al. 1997; Burk et al. 1999), and is run operationally by the U.S. Navy in several coastal areas of the globe to provide real-time forecasts. COAMPS has nested-grid capability and uses multivariate optimum interpolation analysis to map the observations to its grid. Details can be found in Hodur (1997).

COAMPS simulations require the Navy Operational Global Atmospheric Prediction System (NOGAPS) outputs produced by the Fleet Numerical Meteorology and Oceanography Center (FNMOC). The NOGAPS datasets with 1° resolution are interpolated to the COAMPS domain grids as a first guess. The first-guess
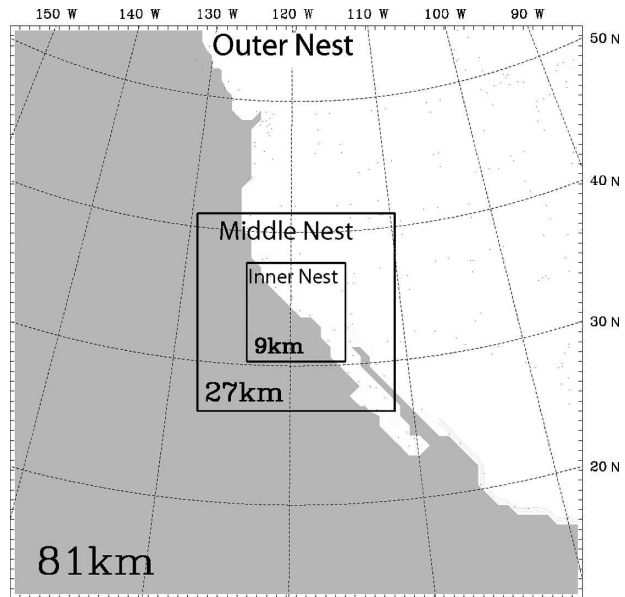

FIG. 2. The triple-nest configurations of COAMPS used in the present study; the outer nest has $\Delta = 81$ km, the middle nest has $\Delta = 27$ km, and the inner nest has $\Delta = 9$ km.

fields are then enhanced by observations: radiosondes, surface stations, and aircraft reports. Incremental assimilation is used every 12 h to incorporate the observations.

The model topography is derived from the Defense Mapping Agency's 100-m resolution dataset subsampled to 1-km resolution, while sea surface temperature (SST) is obtained through an optimum interpolation analysis of FNMOC SST on the COAMPS domain (details in Chen et al. 2003). A triply nested domain is configured with one-way interaction between the outer (with horizontal grid size = $\Delta = 81$ km), middle ($\Delta = 27$ km), and inner ($\Delta = 9$ km) domains centered over the SBC (Fig. 2). The model top is 31 km and there are 30 unevenly spaced vertical sigma levels, with 11 levels in the lowest 1.6 km, down to 10 m for the grid nearest the ocean surface. The Kain–Fritsch cumulus parameterization is only used on the two outer nests.

3. Model mean fields

We focus on the inner-nest ($\Delta = 9$ km) results but will examine grid sensitivity using the $\Delta = 27$- and 81-km grids. We solely use the 10-m wind (hereafter referred to as "the wind") outputs at the lowest sigma level. To compare COAMPS with winds from buoy stations and other products, Large and Pond's (1981) bulk formula is used to compute wind stresses from all the

different wind velocities, including those from ECMWF, observation stations, and our own reanalysis wind product "SEB" (see section 4b). We first discuss the 3-month-averaged fields, then the monthly and shorter time-scale results.

a. Three-month (March–May) averages

Figure 3 shows the averaged (March–May) wind speed (top panel) and wind stress curl (bottom panel) in the inner nest. The mean wind off the central and northern California coast is from the north-northwest almost parallel to the coastline, with wind speeds > 6 m s^{-1}. Winds rapidly decrease near the coast within a cross-shore width of about 50–100 km, with wind speeds ≈ 1–2 m s^{-1} over land (not shown). Inside the SBC and in the SoCB, the wind veers cyclonically such that it is blowing almost onshore in the SoCB and weakens. These features generally agree with observations (Winant and Dorman 1997). The stronger upwelling-favorable wind (stress) off the central and northern California coast is known to produce equatorward currents and cool waters near the coast (e.g., Beardsley and Lentz 1987), but upwelling is weaker in the southern California Bight (Harms and Winant 1998).

Figure 3 also shows that flows accelerate downwind of Point Sur, Point Conception, and the westernmost channel islands, San Miguel and Santa Rosa; maximum mean speeds ≈6–8 m s^{-1}. Koračin and Dorman (2001) found similar maxima in the lee of major capes, and minima upstream using the fifth-generation Pennsylvania State University–National Center for Atmospheric Research Mesoscale Model (MM5). They show that the maxima generally coincide with (surface) flow divergence while there is convergence upstream and immediately in the lee of the cape near the coast. We find similar features in the COAMPS divergence field (not shown). The wind stress curl maximizes downwind of these capes and western islands, with values ≈ 0.3–0.5 N m^{-2} (100 km)$^{-1}$, and ≈1 N m^{-2} (100 km)$^{-1}$ south of Point Sur (Fig. 3). Perlin et al. (2004) obtained similar values from a COAMPS (Δ = 9 km) simulation off the Oregon–California coast (downwind of Cape Blanco; see their Fig. 20). In the SBC, the wind maximizes near the channel's center resulting in a strong cyclonic curl in the northern two-thirds of the channel; in the southern third, the curl changes sign to become anticyclonic, though much weaker (cf. observations by Dorman and Winant 2000). The strong cyclonic curl in the channel is in part responsible for the spinup of a cyclone in the ocean in the western portion of the channel, especially in spring (Oey 1999; Munchow 2000; Oey et al. 2004). On a larger scale, southward along the coast of the
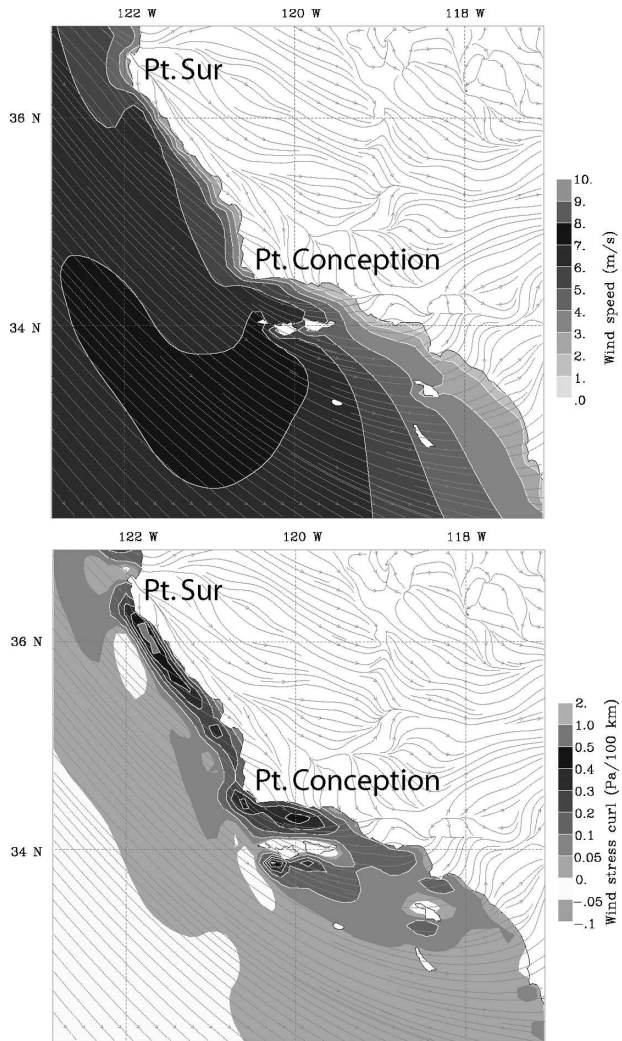

Fig. 3. Contours of 3-month-averaged (March–May 1999) COAMPS (top) wind speed and (bottom) wind stress curl in the inner nest (Δ = 9 km) at the lowest sigma point (10 m over the ocean). Surface streamlines indicating flow directions are superimposed on each panel, but for clarity, overland contours are omitted.

SoCB, the cyclonic wind stress curl continuously weakens, to less than 0.05 N m^{-2} (100 km)$^{-1}$ at 32°N. This equatorward weakening has been shown to be important forcing that in part determines the along-coast ocean currents (Oey 1996, 1999).

By comparing middle- and inner-nest fields we can check the effects of resolution. The middle-nest winds are smoother though speeds (not shown) do not differ much from the inner nest. As can be expected, the largest contrast is in wind stress curl (and divergence). Figure 4 shows the 3-month-averaged wind stress curl from the middle nest (Δ = 27 km), which should be compared with Fig. 3 (bottom panel) for the inner nest (Δ = 9 km). Note the contrast in near-coast distributions and
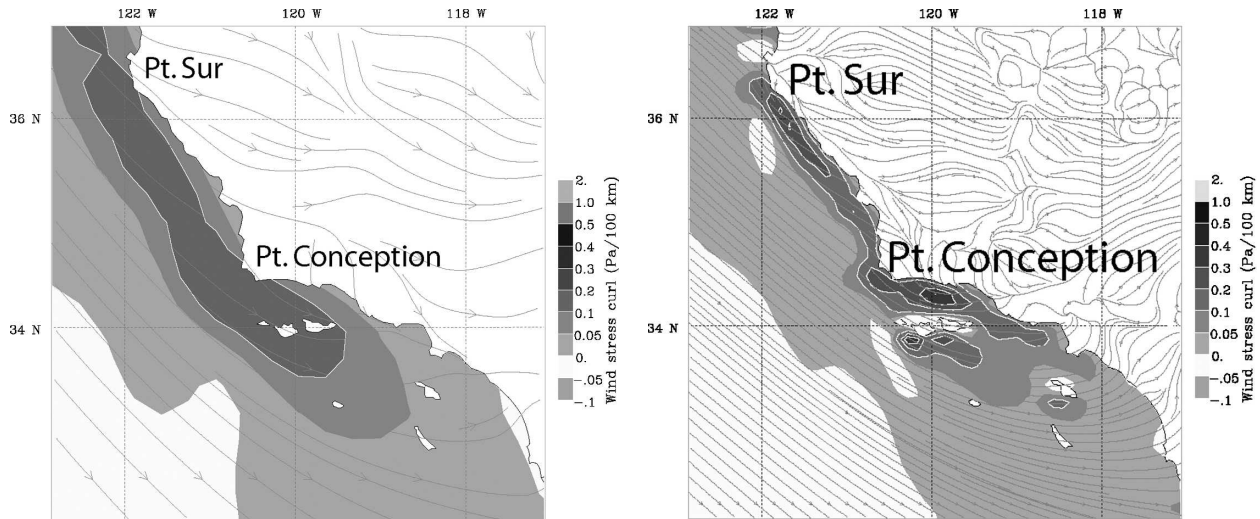
FIG. 4. Contours of 3-month-averaged (March–May 1999) COAMPS wind stress curl in the middle nest ($\Delta = 27$ km) at the lowest sigma point (10 m over the ocean). Surface streamlines indicating flow directions are superimposed, but for clarity, overland contours are omitted.

magnitudes. Largest wind stress curls in the middle nest spread over 75 km cross shore, compared with the inner-nest distribution that has about half the scale and magnitudes that are approximately 2–3 times more intense. This grid sensitivity may be compared with Perlin et al. (2004). These authors showed that wind stress curls calculated from the Quick Scatterometer (Quik-SCAT) satellite data and from the National Centers for Environmental Prediction 32-km hydrostatic Eta Model output gave values that are 3–5 times weaker than their inner-nest COAMPS run. In QuikSCAT, near-coast (≈ 50 km) data had to be omitted. For the Eta Model, the lower values were most likely a result of lower resolution. Below we will examine wind distributions from relatively dense arrays of observations that show maximum wind stress curls near the coast, with similar scales and strengths as the inner-nest curls. These results emphasize the importance of using good resolution especially near the coast.

b. Monthly means

The northwesterly wind strengthens from March to May (not shown) because of the eastward progression of the subtropical high over the eastern Pacific coupled with development of a low over the southwestern United States (Dorman and Winant 2000). Increased wind strengths in April and May contribute to increased upwelling off central and northern California (Beardsley and Lentz 1987), and also over the western SBC (Harms and Winant 1998). Figure 5 shows subtle
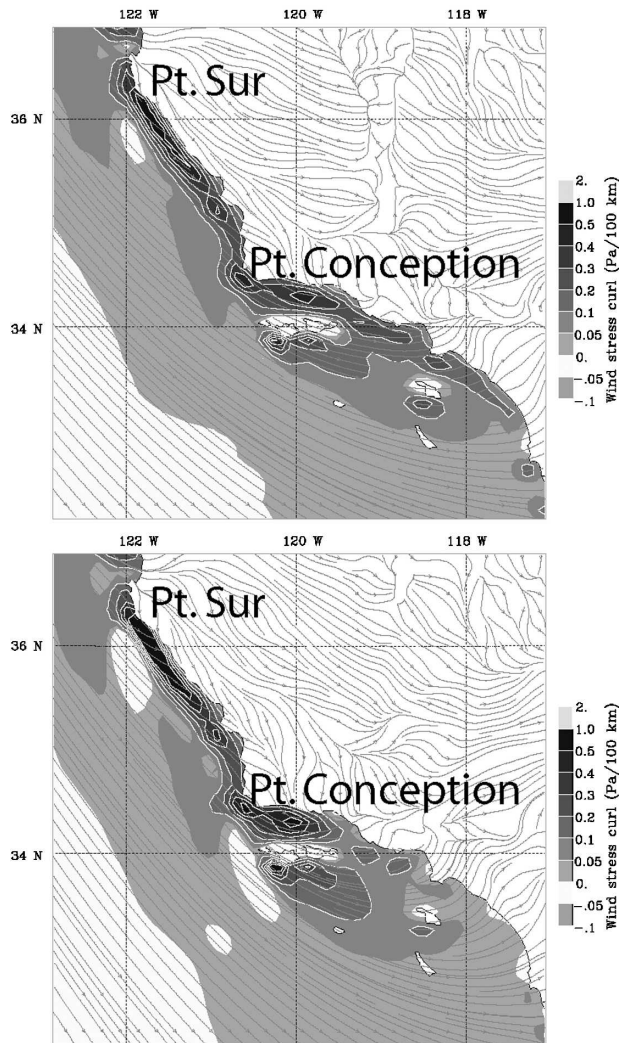

FIG. 5. Contours of monthly averaged, March–May 1999, COAMPS wind stress curl in the inner nest ($\Delta = 9$ km) at the lowest sigma point (10 m over the ocean). Surface streamlines indicating flow directions are superimposed, but for clarity, overland contours are omitted.

changes in the monthly wind stress curl near the coast. Changes over the open ocean are much less. In the eastern channel and in SoCB, wind stress curls (and wind speeds) strengthen from March to April then weaken in May. In contrast, wind off the CCSS strengthens continuously with time. The transition of wind characteristic from winter to late spring and summer will be described in more detail below in conjunction with observations.

4. Quantitative assessments and grid sensitivity

a. Comparison with surface station observations

We compare model output against wind time series at the stations shown in Fig. 1. We focus on stations in the vicinity of the SBC where the largest discrepancies between model and observations are found. Because of the sharp bend in the coastline, flows in the SBC would entail small-scale dynamics that can be sensitive to grid resolution. We therefore also compare the inner- and middle-nest solutions. Figure 6 plots the principal axis (PA; PA is the directional axis containing the maximum observed variance in the flow, i.e., wind in the present case; Harms and Winant 1998) winds observed (solid curves) at the six stations B23, B54, ROSA, B53, GAIL, and B25 (for locations see Fig. 7).[1] The modeled winds (dotted for the middle nest and dashed for the inner nest), to be discussed later, are also plotted. Positive PA is poleward and the PA angles are indicated in each panel. Figure 7 gives the corresponding variance ellipses and mean winds at these and four other stations. Equatorward winds generally prevail. However, at B23 and B54, two major wind reversals (i.e., poleward) occur in March, on 19 and 25 March, with peaks of approximately 9 and 6 m s^{-1}, respectively, at B23. The reversals extend to eastern and southern stations also, though weaker, and are followed by 10 days of persistently strong equatorward wind ($\approx$10 m s^{-1} at B23 and B54) from the end of March through the beginning of April. Through the rest of April, the strong equatorward wind is punctuated by a series of weakened or even slightly reversed wind events. Note that strong equatorward wind bursts occur more often from late March to April, than earlier times in March, and moreover they extend farther to the southern and eastern stations (B53, GAIL, and to a lesser degree B25 also). In May, winds at the three western stations become more persistently equatorward during the first

three weeks before it weakens (following a wind reversal on 23 May) near the end; winds are weak at the three eastern and southeastern stations.

In summary, the observed winds in March–April 1999 are more coherent throughout the channel; that is, strong or weakened (at times reversed) equatorward winds in the west coincide with similar events in the east. In early May 1999, the characteristics change quite abruptly (within one week) when winds in the east and southeast (in the SoCB) weaken, while winds west and north intensify and become more persistently equatorward. This latter characteristic is typical of the summertime winds (Dorman and Winant 2000). The shift in (wind) behavior from the transition of spring to summer in 1999 can be seen in plots of correlation coefficients between west–east station pairs: B54 and GAIL, and also B54 and B53, as shown by the solid curves in Fig. 8. (Modeled correlations, to be discussed shortly, are also plotted.) The correlations are calculated using a 15-day moving window, and the 95% significance curves are also shown. The correlations between B54 and eastern stations are significant and relatively high (generally >0.6) in March and April but drop below 0.4 and also below the 95% significance curve in early May. In terms of the ocean response, Dong and Oey (2005) show that the equatorward wind bursts that span the entire channel in early spring of 1999 triggers equatorward currents (see also Harms and Winant 1998; Oey et al. 2001, 2004). By late spring and early summer, in May, the weakened winds to the east and south, coupled with persistent equatorward winds in the west, sets up an along-channel pressure gradient that in part induces poleward coastal current along the northern coast of the channel (cf. Oey et al. 2004).

The time series comparison between the modeled and observed winds (Fig. 6) shows that the model does well in reproducing the observed fluctuations in March and April, but rather poorly in May. Modeled variances and mean wind vectors (Fig. 7) are in general agreement though the model tends to underestimate (overestimate) the intensity and PA angle in the west (east). The proximity of modeled to observed time series is measured in Fig. 9 in terms of model-observed correlation and skill (Sk) at the 10 stations. The skill is defined as (cf. Davis 1976)

$$Sk = [1 - \langle(\mathbf{u}_m - \mathbf{u}_o) \cdot (\mathbf{u}_m - \mathbf{u}_o)\rangle/\langle\mathbf{u}_o \cdot \mathbf{u}_o\rangle],$$

where $\langle\ \rangle$ is time averaging over the 3-month period, $\mathbf{u}$ denotes the wind vector, and subscripts m and o denote the model and observation, respectively. Values of Sk = 1 represent a perfect match between model and observations. It is seen that both correlation and skill

---

[1] Reference to the National Data Buoy Center (NDBC) stations will often be simply the last two digits preceded by "B" (e.g., B54 for 46054).
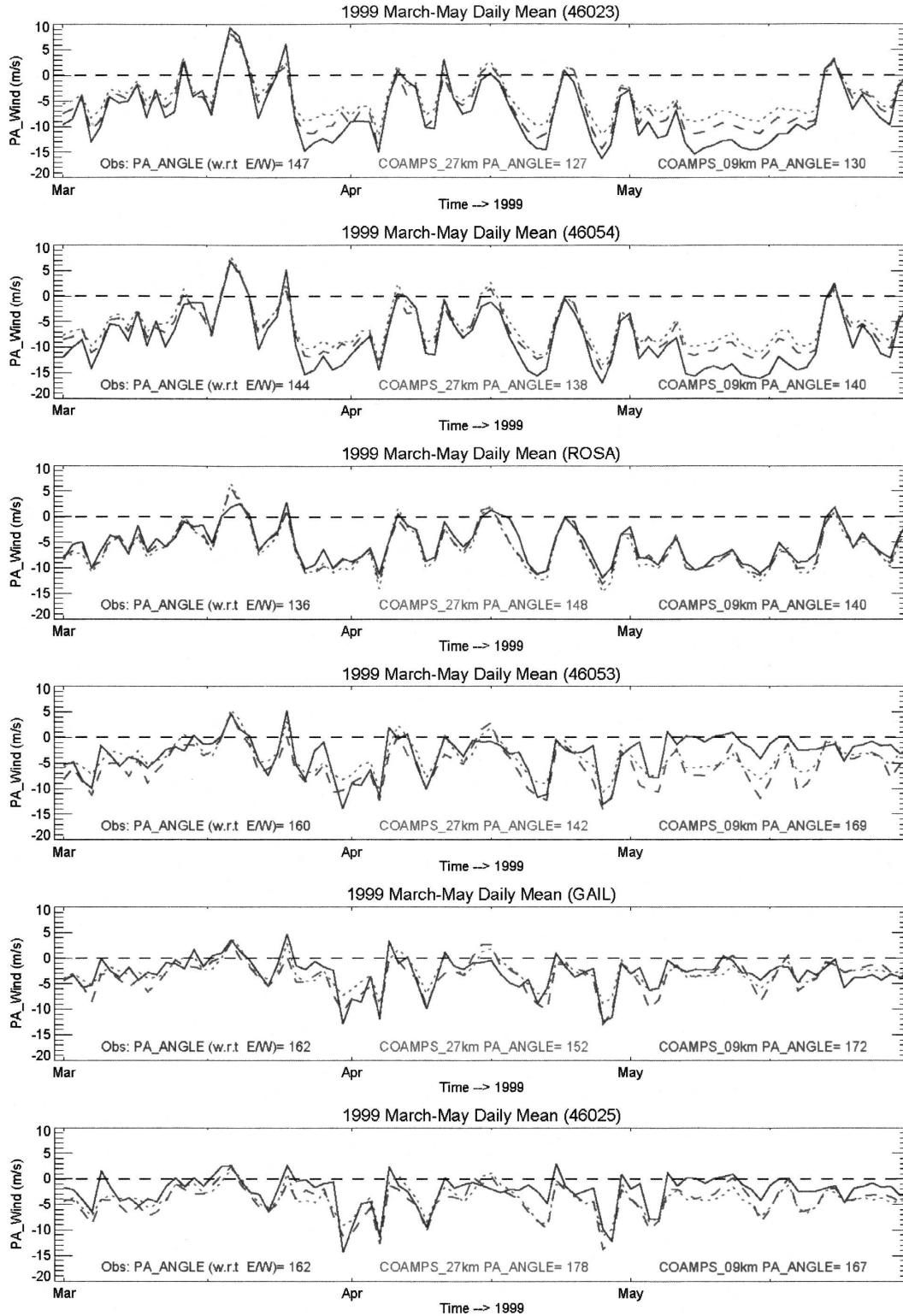
FIG. 6. Wind time series from March to May 1999, shown here as daily averaged PA values at six NDBC and coastal stations arranged from (top) north to (bottom) south: 46023, 54, ROSA, 53, GAIL, and 25 (please see Fig. 7 for locations). The PA angles, measured in degrees anticlockwise from true east, are printed in each panel. Solid curves are observed, dotted curves are modeled from the middle nest ($\Delta = 27$ km), and dashed curves are modeled from the inner nest ($\Delta = 9$ km).
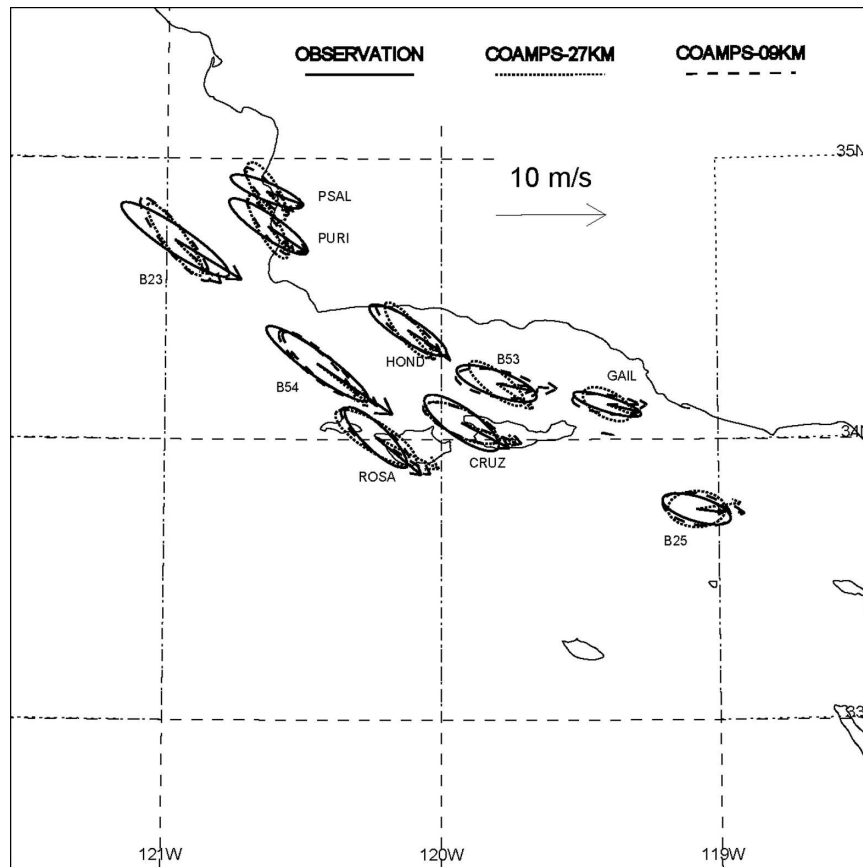
FIG. 7. Wind PA ellipses at the 10 indicated stations in the vicinity of the SBC, for the period March–May 1999. The wind vectors are also shown. Solid lines are observed, dotted lines are modeled from the middle nest (Δ = 27 km), and dashed lines are modeled from the inner nest (Δ = 9 km).

are quite high (>0.7) for the western stations, but low for the eastern and southeastern stations (especially at B53 and B25). The finer grid (Δ = 9 km) tends to give better results but the skills for the coarser grid (Δ = 27 km) are slightly higher in the eastern portion of the channel. The finer grid does give closer agreement (with the observed; Figs. 6 and 7) in the PA angles. Figure 6 indicates that the poor skill and correlation at B53 are because the model overestimates winds during May. If May is excluded, the correlation and skill both increase to about 0.9. On the other hand, if only May is used, the correlation drops to ∼0.4 and a negative skill is obtained. The overestimation of wind at B53 during May is related to the results in Fig. 8 that modeled winds over the western and eastern portions of the channel are more correlated than they should be according to observations; the modeled west–east correlations are larger than observed at all times (Fig. 8). In other words, the modeled "eddy" or spatial correlation scale is larger than observed. Dorman and Winant

(2000) suggest that winds in the eastern channel are affected by local airflows from land. Details of the local flows depend on accurate modeling of the planetary boundary layer (PBL) over finescale orography, which are easily misrepresented by insufficient model resolution. A supercritical expansion fan around Point Conception over the western channel also exists (Dorman and Winant 2000; Skyllingstad et al. 2001; see also Dorman 1985a; Winant et al. 1988; Samelson 1992; Haack et al. 2001). The expansion fan is followed by compression waves somewhere in the midchannel, near B53 (as inferred from the observed time series in Fig. 6, which shows abruptly weakened wind from B54 and Rosa to B53 after May). The transition from strong to weak wind occurs over a distance of (at most) half the channel's length (≈50 km), which is not resolved well by the COAMPS grid (see also Fig. 10). Dynamically, the modeled wind in the east is part of the same Pacific pressure system as the wind in the west. While this situation is generally correct in March and April, it no
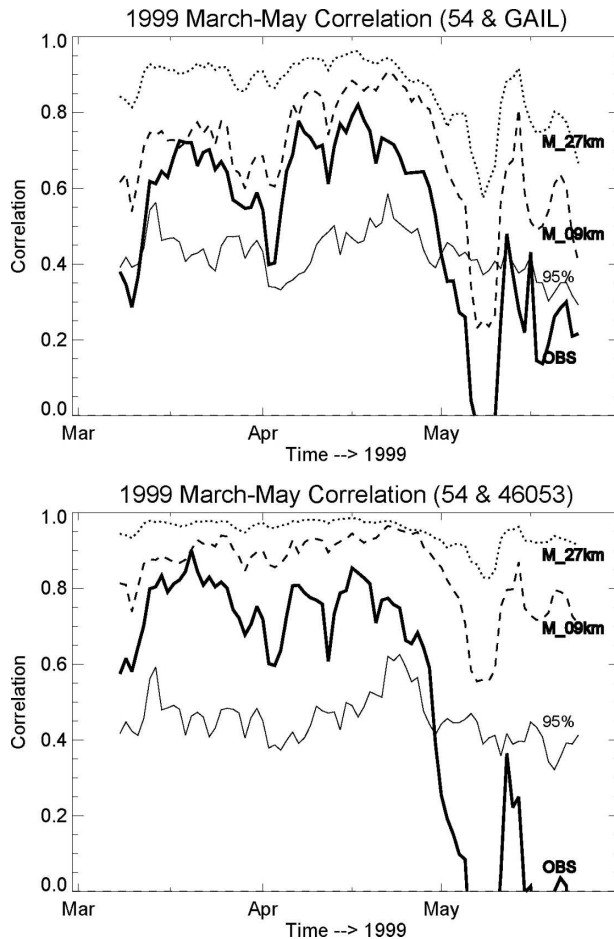
FIG. 8. Correlations between (top) B54 and GAIL and (bottom) B54 and B53 during March–May 1999. Solid curves are observed, dotted curves are modeled from the middle nest (Δ = 27 km), and dashed curves are modeled from the inner nest (Δ = 9 km). The 95% significance level curve is also plotted. The correlation was computed using a 15-day moving window.
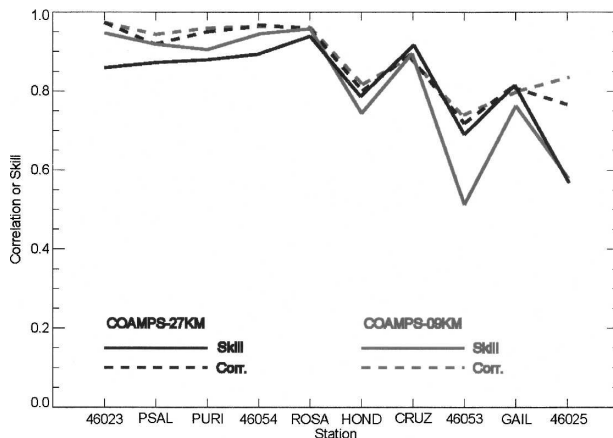

FIG. 9. Correlations (dash) between the observed and modeled PA winds at the indicated 10 stations in the vicinity of the SBC. The corresponding skills (solid) are also shown. Dark lines are modeled from the middle nest (Δ = 27 km) and gray lines are modeled from the inner nest (Δ = 9 km).

longer holds in May when observations show a distinct disconnect between east and west (Fig. 8). Figure 8 indicates that the model results improve in the inner nest. However, an even finer grid is necessary to resolve the detailed topography and to correctly simulate compression waves in the channel.

The observed wind weakening from west to east (Fig. 6) may also be due to the existence of the so-called Catalina eddy, which produces weak reversed flow (i.e., southerly winds of a few meters per second) near the southern California coast (Davis et al. 2000). The eddy has scales of $O(100$ km), is rather thin (approximately 1–2 km above the mean sea level), and can last for a few days. Davis et al.'s 6.7-km simulation using the MM5 shows the reversed flows on 26–30 June 1988 (see their Fig. 2) and our 9-km COAMPS simulation also appears to show similar large-scale features in mid-May 1999

(see below). However, observations presented in Dorman and Winant (2000) do not support the idea that the Catalina eddy influences the wind variability in the eastern portion of the channel (at B53 and GAIL). Figure 6 also shows no such flow reversals (or very weak and brief if any) at B53 and GAIL during May. Dorman and Winant (2000) show that summer winds are predominantly from the west. Moreover, they show that only on 23% of the summer days have both GAIL and B53 a component from the east-southeast in excess of 1 m s^{-1}. Their results are in good agreements with our May 1999 data at B53 and GAIL, and do "not support the dominance of a midchannel eddy" (Dorman and Winant 2000). The observations instead suggest complex local winds in the middle to eastern channel; these winds do not correlate well with winds in the western channel. Dorman and Winant (2000) also found that observations at B54 and B53 are only weakly correlated (cf. Fig. 8).

b. Comparison with reanalysis—The SEB

We extend the pointwise time series comparison (above) to yield information on spatial variability by comparing COAMPS and observed wind and wind stress curl maps. The observed maps are derived by combining satellite, ECMWF, and buoy (NDBC and coastal) wind data—referred to as the SEB dataset, as follows. The SSM/I data are produced as part of the National Aeronautics and Space Administration Pathfinder Program. A unified, physically based algorithm is used to simultaneously retrieve ocean wind speed (at 10 m), water vapor, cloud water, and rain rate (Wentz

1997; Wentz and Spencer 1998). Only the wind speed portion of the data is used for our purpose. Three-day-averaged fields on ¼° × ¼° grid were used. The original data already have a near-coast strip of width ≈50 km omitted, but a further quality check was necessary to remove bad data at grid points where speeds and spatial gradients were unrealistically high. The data were then checked against the ECMWF reanalysis product on 1.125° Gaussian grid by computing the correlation between the two speed products over the period from 1992 to 1999. The correlation was found to be good (coefficients ≈0.8) over the open ocean, some 100 km off the coast (not shown). There is also good agreement between SSM/I and offshore NDBC winds. The agreements between ECMWF u and v winds and NDBC winds were also found to be excellent in the phasing, though the ECMWF speeds were too low within 100 km of the coast. We therefore keep the ECMWF wind directions at offshore locations but replace the speeds using the SSM/I data. The combined SSM/I and ECMWF product was then used with all available wind data (stations in Fig. 1) to optimally interpolate (OI) onto Oey et al.'s (2001) ocean domain (as shown by the rectangle in Fig. 1) using 5 km × 5 km grid sizes at 6-hourly intervals from 1993 to 1999. This final product is the SEB dataset. The radius of influence for OI is R_{OI} = 50 km, approximately the width of the channel. In the regions of interest, the SBC and CCSS, there is a sufficient number of buoys (Fig. 1) so that R_{OI} = 50 km ensures that the resulting wind product (SEB) is locally dominated by the buoy data.

Figure 10 compares the ECMWF, COAMPS (Δ = 9 km), and SEB wind stresses and wind stress curls averaged over March–May 1999, focusing on the SBC and CCSS. In this small domain the ECMWF wind speed is weak in comparison to COAMPS and SEB. The ECMWF direction off CCSS is comparable to the higher-resolution COAMPS, but there is less onshore (or eastward) turning (than COAMPS) in the SoCB. Note that away from the coast, SEB incorporates ECMWF wind directions into the OI analysis and therefore also gives little turning in the SoCB. However, in the eastern portion of the SBC where the SEB analysis is dominated by observations, the ECMWF wind also shows less turning than both COAMPS and SEB. The ECMWF wind stress curl is also weaker than COAMPS and SEB especially near the coast where values of about 0.5 Pa $(100 \text{ km})^{-1}$ may be seen in COAMPS and SEB results. The ECMWF wind field is actually very similar to the COAMPS field from the outer grid (Δ = 81 km; not shown). Clearly, the ECMWF (or the coarse-grid COAMPS) wind is inadequate for use in ocean simulation in the CCSS–SBC–SoCB region (Dong and Oey 2005).

Both COAMPS and SEB give similar wind speeds, though COAMPS is somewhat stronger farther offshore. SEB also shows a maximum speed just west of the channel while the COAMPS maximum is located farther downwind south of the channel islands. The most important difference, however, is in the spatial distribution of the wind stress curl. In the channel, the SEB strong curl is concentrated in the western portion, while for COAMPS the region of strong curl extends farther eastward. This result is consistent with Fig. 8 in that the COAMPS wind shows stronger west–east correlations than the observations. The SEB also shows a localized wind stress curl maximum immediately downwind of Point Buchon (please see Fig. 1 for location), while the COAMPS wind stress curl tends to show a more coherent along-coast structure. Dong and Oey (2005) show that the coastal ocean currents are sensitive to these subtle differences in the wind stress curl. We emphasize that the SEB localized wind stress curls in Fig. 10 are not artifacts of the OI. There is a sufficient number of buoys near the coast and tests with R_{OI} = 75 and 100 km (rather than 50 km) give virtually identical results; moreover, the SSM/I data are good for distances greater than about 50 km from the coast. The near-coast occurrence of wind maximum appears to be a robust feature that occurs also in COAMPS at 9-km resolution, as well as in other analyses (e.g., Koračin and Dorman 2001; Perlin et al. 2004).

5. Wind turning in the Southern California Bight

We pointed out above that ECMWF (and coarse-grid COAMPS) winds do not show large-scale eastward turning in the SoCB, in contrast to winds from fine-grid COAMPS and the observed climatology (Winant and Dorman 1997). One possible explanation is that the turning is the cumulative effect of synoptic cyclones produced south of Point Conception. Note however that these cyclones are not the very small scales inside the SBC, discussed in the previous section. They are larger scales that fill the SoCB, and appear to be well resolved by inner-nest COAMPS at the Δ = 9-km resolution. Figure 11 shows an example on 1300 UTC 18 May with the inner-nest COAMPS wind at 10 m superimposed on the corresponding map of vorticity. A detailed analysis (not shown) indicates that the development of cyclones downwind of Point Conception are generally preceded by strong equatorward winds over the ocean, off central and northern California in particular. Cyclonic eddies downwind of Point Conception have been observed; they are often referred to as the "Catalina eddies" and there is strong evidence that lee cyclogenesis is usually involved in the generation of
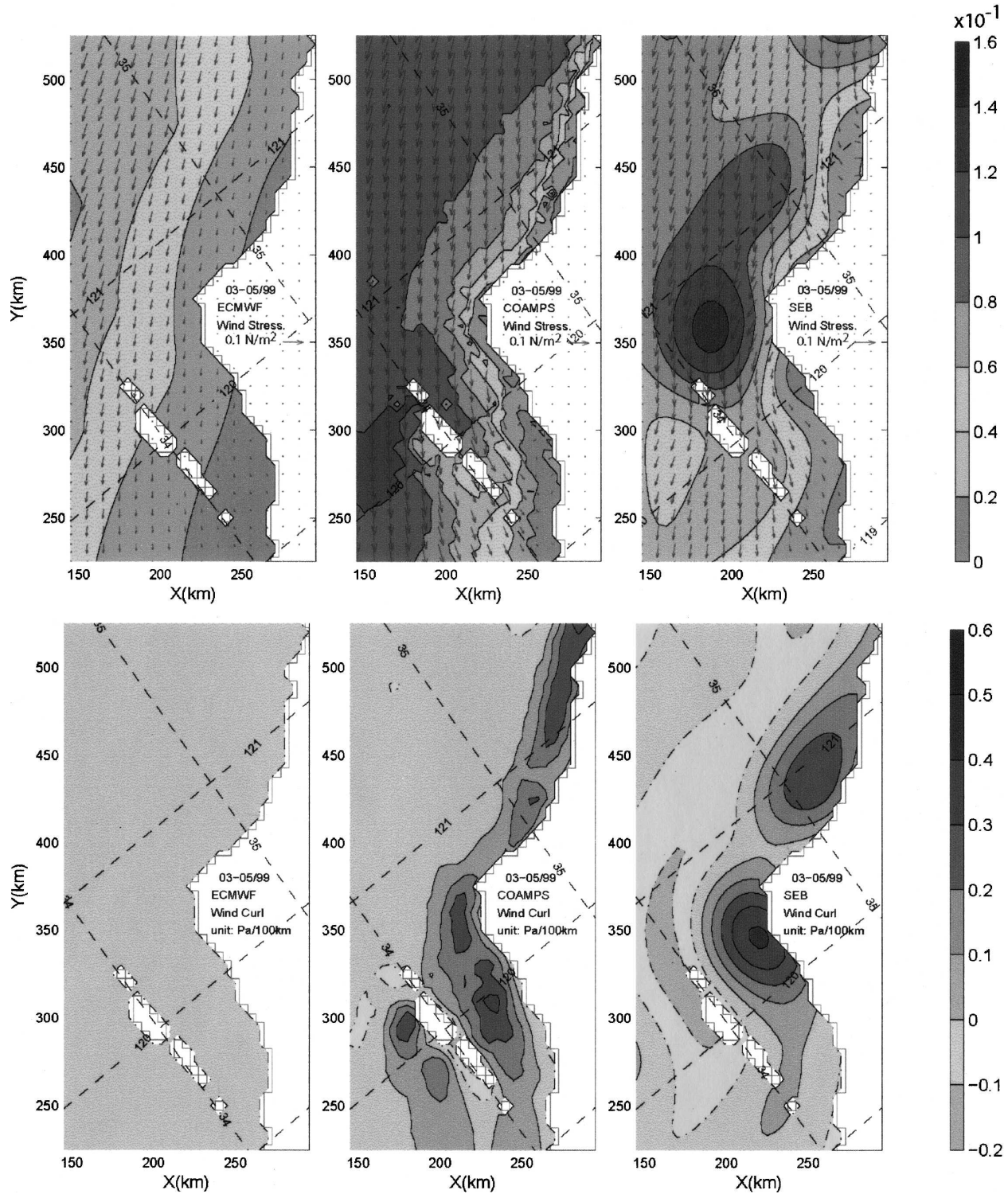
FIG. 10. (top) The 3-month (March–May 1999) mean wind stress vectors obtained from (left) ECMWF, (middle) COAMPS, and (right) SEB. Contours indicate wind stress magnitudes and the contour interval is 0.02 N m^{-2}. (bottom) the 3-month mean contours of the wind stress curl for (left) ECMWF, (middle) COAMPS, and (right) SEB. The contour interval is 0.2 Pa (100 km)$^{-1}$. The domain is enlarged focusing on the SBC and CCSS, and tilted 52° anticlockwise from north as in the model domain shown in Fig. 1. Dashed lines are latitudes and longitudes in the indicated degrees.
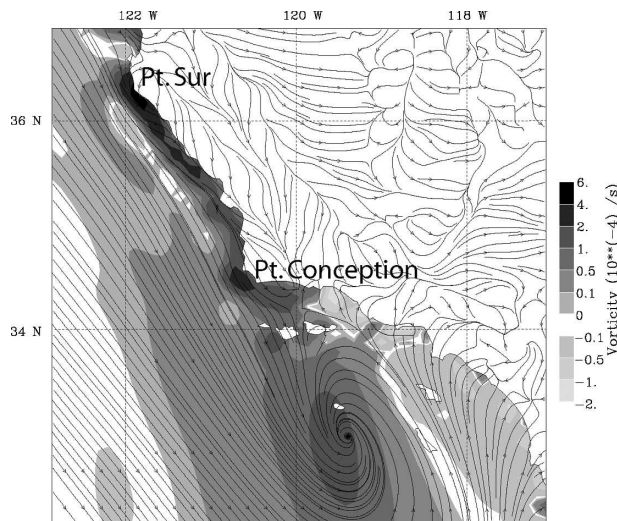
FIG. 11. COAMPS (inner nest with $\Delta = 9$ km) 10-m wind streamlines superimposed on a grayscale map of vorticity at 1300 UTC 18 May 1999. This shows the development of cyclones downwind of Point Conception.

these eddies (Rosenthal 1968; Bosart 1983; Dorman 1985b; Wakimoto 1987; Mass and Albright 1989; Clark and Dembek 1991; Ueyoshi and Roads 1993; Clark 1994).

6. Summary

Accurate wind information is necessary to simulate ocean currents. Both wind stress and wind stress curl, in part, determine the internal pressure distribution of the ocean. This paper applies a regional atmospheric model, COAMPS, at moderately high resolution ($\Delta = 9$ km) to simulate winds off the central and southern California coast, the SBC in particular. We check COAMPS against observations for the period March–May 1999. This is a spring transition period when the wind changes from its characteristics more typical of winter with storm passages in early March, through April–May when there exist more persistent and intense equatorward winds off the central California coast and weak winds in the eastern portion of the SBC and also in the SoCB. The complexity of the wind field poses a challenge to any model.

We compare COAMPS with the wind time series from ocean and land stations. The agreements are good during March and April, but poor in May especially for stations in the eastern SBC. At the highest resolution used here ($\Delta = 9$ km), the model still fails to accurately simulate wind dynamics in the channel. Strong curls are observed across the channel's half-width of only approximately 20–25 km, and also along the channel (Fig.

10). Therefore there are at most approximately 1–5 grids for the COAMPS's *finest* 9-km inner nest. This resolution is not sufficient (Richtmyer and Morton 1957; Isaacson and Keller 1966). The modeled winds east and west of the SBC are part of the same large-scale system over the open ocean, rather than uncorrelated as observed. On the other hand, the results from $\Delta = 9$ km are better than those from $\Delta = 27$ km, which suggests improved model skill with further grid refinement incorporating high-resolution topography. At the refined resolution, future work should also test the model sensitivity to various parameterizations such as the PBL physics.

COAMPS results (at $\Delta = 9$ km) also show flow expansions behind coastal promontories (capes) and enhanced wind stress curls near coast. The along-coast curl field from the model, however, exhibits more along-coast coherence than suggested by the observations. On a larger scale, COAMPS wind speeds over the open ocean are in fair agreements with those obtained from satellites (SSM/I). Over the SoCB, COAMPS correctly simulates onshore cyclonic turning of the wind in agreement with observations. This is in contrast to coarser-grid ECMWF reanalysis wind (on a 1.125° Gaussian grid) and also to the outer-nest ($\Delta = 81$ km) COAMPS wind, both of which give little turning. COAMPS simulation suggests that the onshore turning is in part driven by cyclonic "eddies" downwind of Point Conception. These eddies are typically preceded by a few days of strong equatorward winds over the central California coast and open ocean and appear to be related to the troughing in the lee of the high terrain north of Santa Barbara. Figure 11 shows that the cyclone contributes to poleward flow over the eastern portion of the SoCB and SBC. It is therefore possible that COAMPS does not produce a sufficient number of Catalina eddies, so that the modeled winds east and west of the channel are more correlated than observed (Fig. 8). This needs further research. Finally, the modeled wind stress curl along the coast in the Southern California Bight decreases toward the south; this decrease is in part responsible for poleward surface currents found in the observations and models (e.g., Harms and Winant 1998; Oey 1996, 1999).

In an accompanying paper (Dong and Oey 2005), the above COAMPS winds are used in ocean hindcast experiments. The authors compare the (model) ocean responses to various winds including COAMPS (in detail with the observations). They compute momentum balance, EOFs, and conclude that COAMPS winds at $\Delta = 9$-km resolution are inadequate in explaining the observed (oceanic) jet off the central California coast. This (ocean) result further supports our inferences that

the 9-km COAMPS still lacks the resolution required to "characterize some oceanographically relevant aspects of meteorological variability."

REFERENCES

Allen, J. S., 1980: Models of wind-driven currents on the continental shelf. *Annu. Rev. Fluid Mech.,* **12,** 389–433.

Beardsley, R. C., and S. J. Lentz, 1987: The Coastal Ocean Dynamics Experiment collection: An introduction. *J. Geophys. Res.,* **92,** 1455–1463.

Bosart, L. F., 1983: Analysis of a California Catalina eddy event. *Mon. Wea. Rev.,* **111,** 1619–1633.

Brink, K. H., and R. D. Muench, 1986: Circulation in the Point Conception-Santa Barbara Channel region. *J. Geophys. Res.,* **91,** 877–895.

Burk, S. D., T. Haack, and R. M. Samelson, 1999: Mesoscale simulation of supercritical, subcritical, and transcritical flow along coastal topography. *J. Atmos. Sci.,* **56,** 2780–2795.

Caldwell, P. C., D. W. Suart, and K. H. Brink, 1986: Mesoscale wind variability near Point Conception, California during spring 1983. *J. Climate Appl. Meteor.,* **25,** 1241–1254.

Chen, S., and Coauthors, 2003: COAMPS™ version 3 model description: General theory and equations. Naval Research Laboratory, Monterey, CA, 143 pp.

Clark, J. H. E., 1994: The role of Kelvin waves in evolution of the Catalina eddy. *Mon. Wea. Rev.,* **122,** 838–850.

——, and S. R. Dembek, 1991: The Catalina eddy event of July 1987: A coastally trapped mesoscale response to synoptic forcing. *Mon. Wea. Rev.,* **119,** 1714–1735.

Davis, C., S. Low-Nam, and C. Mass, 2000: Dynamics of a Catalina eddy revealed by numerical simulation. *Mon. Wea. Rev.,* **128,** 2885–2904.

Davis, R. E., 1976: Predictability of sea surface temperature and sea level pressure anomalies over the North Pacific Ocean. *J. Phys. Oceanogr.,* **6,** 249–266.

Dong, C., and L.-Y. Oey, 2005: Sensitivity of coastal currents near Point Conception to forcing by three different winds: ECMWF, COAMPS, and blended SSM/I–ECMWF–Buoy winds. *J. Phys. Oceanogr.,* **35,** 1229–1244.

Dorman, C. E., 1985a: Evidence of Kelvin waves in California's marine layer and related eddy generation. *Mon. Wea. Rev.,* **113,** 827–839.

——, 1985b: Hydraulic control of the northern California marine layer. *Eos, Trans. Amer. Geophys. Union,* **66,** 914.

——, and C. D. Winant, 1995: Buoy observations of the atmosphere along the west coast of the United States, 1981–1990. *J. Geophys. Res.,* **100,** 16 029–16 044.

——, and ——, 2000: The structure and variability of the marine atmosphere around the Santa Barbara Channel. *Mon. Wea. Rev.,* **128,** 261–282.

Doyle, J. D., 1997: The influence of mesoscale topography on a coastal jet and rainband. *Mon. Wea. Rev.,* **125,** 1465–1488.

Haack, T., S. D. Burk, C. E. Dorman, and D. P. Rogers, 2001: Supercritical flow interaction within the Cape Blanco–Cape Mendocino orographic complex. *Mon. Wea. Rev.,* **129,** 688–708.

Harms, S., and C. D. Winant, 1998: Characteristic patterns of the circulation in the Santa Barbara Channel. *J. Geophys. Res.,* **103C,** 3041–3065.

Hodur, R., 1997: The Naval Research Laboratory's Coupled Ocean/Atmosphere Mesoscale Prediction System (COAMPS). *Mon. Wea. Rev.,* **125,** 1414–1430.

Harshvardhan, D. Randall, and T. Corsetti, 1987: A fast radiation parameterization for atmospheric circulation models. *J. Geophys. Res.,* **92,** 1009–1016.

Isaacson, E., and H. B. Keller, 1966: *Analysis of Numerical Methods*. John Wiley & Sons, 541 pp.

Kain, J. S., and J. M. Fritsch, 1990: A one-dimensional entraining/ detraining plume model and its application in convective parameterization. *J. Atmos. Sci.,* **47,** 2784–2802.

Koračin, D., and C. E. Dorman, 2001: Marine atmospheric boundary layer divergence and clouds along California in June 1996. *Mon. Wea. Rev.,* **129,** 2040–2056.

Large, W. G., and S. Pond, 1981: Open ocean flux measurements in moderate to strong winds. *J. Phys. Oceanogr.,* **11,** 324–336.

Mass, C. F., and M. D. Albright, 1989: Origin of the Catalina eddy. *Mon. Wea. Rev.,* **117,** 2406–2436.

Munchow, A., 2000: Wind stress curl forcing of the coastal ocean near Point Conception, California. *J. Phys. Oceanogr.,* **30,** 1265–1280.

Oey, L.-Y., 1996: Flow around a coastal bend: A model of the Santa Barbara Channel eddy. *J. Geophys. Res.,* **101C,** 16 667–16 682.

——, 1999: A forcing mechanism for the poleward flow off the southern California coast. *J. Geophys. Res.,* **104C,** 13 529–13 539.

——, D.-P. Wang, T. Hayward, C. Winant, and M. Hendershott, 2001: Upwelling and cyclonic regimes of the near-surface circulation in the Santa Barbara Channel. *J. Geophys. Res.,* **106C,** 9213–9222.

——, C. Winant, E. Dever, W. Johnson, and D.-P. Wang, 2004: A model of the near-surface circulation of the Santa Barbara Channel: Comparison with observations and dynamical interpretations. *J. Phys. Oceanogr.,* **34,** 23–43.

Perlin, N., R. M. Samelson, and D. B. Chelton, 2004: Scatterometer and model wind and wind stress in the Oregon–northern California coastal zone. *Mon. Wea. Rev.,* **132,** 2110–2129.

Persson, P. O. G., P. J. Neiman, and B. Walter, 2005: Contributions from California coastal-zone surface fluxes to heavy coastal precipitation: A CALJET case study during the strong El Niño of 1998. *Mon. Wea. Rev.,* **133,** 1175–1198.

Richtmyer, R. D., and K. W. Morton, 1957: *Difference Methods for Initial-Value Problems*. Interscience Publishers, 405 pp.

Rosenthal, J., 1968: A Catalina eddy. *Mon. Wea. Rev.,* **96,** 742–743.

Rutledge, S. A., and P. V. Hobbs, 1983: The mesoscale and microscale structure of organization of clouds and precipitation in midlatitude cyclones. VIII: A model for the "seeder-feeder" process in warm–frontal rainbands. *J. Atmos. Sci.,* **40,** 1185–1206.

Samelson, R., 1992: Supercritical marine-layer flow along a smoothly varying coastline. *J. Atmos. Sci.,* **49,** 1571–1584.

——, and Coauthors, 2002: Wind stress forcing of the Oregon coastal ocean during the 1999 upwelling season. *J. Geophys. Res.,* **107,** 3034, doi:10.1029/2001JC000900.

Skyllingstad, E. D., P. Barbour, and C. E. Dorman, 2001: The

dynamics of northwest summer winds over the Santa Barbara Channel. *Mon. Wea. Rev.,* **129,** 1042–1061.

Therry, G., and P. LaCarrere, 1983: Improving the eddy kinetic energy model for planetary boundary layer description. *Bound.-Layer Meteor.,* **25,** 63–88.

Thompson, W. T., S. D. Burk, and J. Rosenthal, 1997: An investigation of the Catalina eddy. *Mon. Wea. Rev.,* **125,** 1135–1146.

Ueyoshi, K., and J. O. Roads, 1993: Simulation and prediction of the Catalina eddy. *Mon. Wea. Rev.,* **121,** 2975–3000.

Wakimoto, R., 1987: The Catalina eddy and its effect on pollution over Southern California. *Mon. Wea. Rev.,* **115,** 837–855.

Wang, D.-P., 1997: Effects of small-scale wind on coastal up-

welling with application to Point Conception. *J. Geophys. Res.,* **102C,** 15 555–15 566.

Wentz, F. J., 1997: A well-calibrated ocean algorithm for SSM/I. *J. Geophys. Res.,* **102C,** 8703–8718.

——, and R. W. Spencer, 1998: SSM/I rain retrievals within a unified all-weather ocean algorithm. *J. Atmos. Sci.,* **55,** 1613–1627.

Winant, C. D., and C. E. Dorman, 1997: Seasonal patterns of surface wind stress and heat flux over the Southern California Bight. *J. Geophys. Res.,* **102C,** 5641–5653.

——, R. Beardsley, C. Dorman, and C. Friehe, 1988: The marine layer off northern California: An example of supercritical channel flow. *J. Atmos. Sci.,* **45,** 3588–3605.